Chinese Physics Letters

LETTER

Frequency–Angle Acoustic Beam Steering via Nearly Dispersionless Gradient Metasurfaces

Cite as: Mengru Jiang *et al*. 2026 *Chin. Phys. Lett.* **43** 111001

DOI CSTR

Recommended Articles

Acoustic Bilayer Gradient Metasurfaces for Perfect and Asymmetric Beam Splitting
Jiaqi Quan, Baoyin Sun, Yangyang Fu, Lei Gao, and Yadong Xu
Chin. Phys. Lett. **41**, (2024)

Discrete Ultra-Broadband Perfect Anomalous Reflection in Depth Gradient Metasurfaces
Siyu Gu, Cong Wang, Ziying Gao, Lei Gao, Drolgar, Feng Gao, Shaojun Wang, and Yadong Xu
Chin. Phys. Lett. **42**, 090401 (2025)

Illusion Optics via Phase-Gradient Metasurfaces
Zhaoyao Pan, Jinpeng Yang, and Yadong Xu
Chin. Phys. Lett. **43**, 010401 (2026)

Perfect Confinement of Acoustic Vortex by Phase-Gradient Metacage
Xicheng Fang, Songsong Li, Baoyin Sun, Dongyang Yan, Junyi Yang, Jie Luo, Dongliang Gao, and Yadong Xu
Chin. Phys. Lett. **42**, 034301 (2025)

Phase-Gradient Metasurfaces Based on Local Fabry–Pérot Resonances
Yanyan Cao, Bocheng Yu, Yangyang Fu, Lei Gao, and Yadong Xu
Chin. Phys. Lett. **37**, 097801 (2020)

A series journal of Chinese Physical Society distributed by IOP Publishing

Chinese Physics Letters

Chin. Phys. Lett. **43** 111001 (2026)

LETTER

DOI: 10.1088/0256-307X/43/11/111001
CSTR: 32039.14.0256-307X.43.11.111001

Frequency–Angle Acoustic Beam Steering via Nearly Dispersionless Gradient Metasurfaces

Mengru Jiang(江梦茹)[1], Zhaoyao Pan(潘赵耀)[1], Jiaqi Quan(权家琪)[2,*], Qiming Hu(胡琦明)[1], and Yadong Xu(徐亚东)[1,*]

[1]School of Physical Science and Technology & Jiangsu Key Laboratory of Frontier Material Physics and Devices, Soochow University, Suzhou 215006, China
[2]School of Mathematics and Physics, Anhui Jianzhu University, Hefei 230601, China

[*]Corresponding authors. Email: austqjq@163.com; ydxu@suda.edu.cn

Gradient metasurfaces provide a powerful platform for wavefront and dynamic beam steering of electromagnetic and acoustic waves by introducing the phase-gradient degree of freedom, but they still suffer from narrow steering angles and low efficiency due to inherent dispersion. Here, we theoretically propose and experimentally demonstrate a dispersionless gradient metasurface approach that offers a practical yet powerful route to wide-angle, near-perfect beam steering, overcoming the longstanding trade-off between bandwidth and efficiency in metasurface design. As a proof of concept, we design and fabricate an acoustic metasurface operating at 3430 Hz, which exhibits near-perfect anomalous refraction with an efficiency exceeding 85% over an unprecedented bandwidth of 44.4% (2800–4400 Hz). This performance enables continuous frequency-driven beam steering from 46.5° to 15.8°, covering a 30.7° field of view. Serving as a critical transition between anomalous and normal dispersion, the concept of dispersionless gradient metasurfaces provides a criterion for evaluating the bandwidth limitations of various dispersive counterparts, and establishes a new paradigm for high-performance, frequency-driven dynamic wavefront manipulation.

Dynamic wavefront control, enabling functionalities such as beam steering of electromagnetic or acoustic waves, is essential for applications ranging from LiDAR and optical communications to analog computing and biomedical ultrasound [1–4]. In recent years, phase-gradient metasurfaces (PGMs) have emerged as a compact and efficient platform for this purpose, leveraging their exceptional ability to tailor both the amplitude and phase of wavefronts [5]. By arranging subwavelength elements with spatially varying phase responses, PGMs introduce abrupt phase shifts (APS) covering a full 2π range within each supercell, thereby generating a transverse phase gradient and providing additional momentum along the interface. This mechanism enables anomalous reflection, refraction, and other wavefront transformations via the generalized Snell's law (GSL) [6–10]. However, PGMs are commonly optimized at a single design frequency. As the frequency deviates, the phase and amplitude responses of their constituent meta-atoms diverge from the designed values due to structural dispersion, impedance mismatch, and near-field coupling. Consequently, achieving beam steering with a fixed PGM design remains inherently limited.

To overcome this limitation, efforts have broadly followed two routes: active reconfiguration at a fixed frequency and passive dispersion engineering for broadband operation. The first employs active or reconfigurable PGMs that respond to external stimuli, such as voltage, temperature, or mechanical deformation, to enable real-time beam steering at a fixed operating frequency [11–20]. While effective, these approaches introduce considerable operational complexity and may compromise device stability or fabrication feasibility. The second, more passive strategy leverages dispersion engineering to broaden the intrinsic bandwidth of PGMs [21–35]. By designing broadband PGMs that diffract different frequencies into distinct angles, this approach eliminates the need for external modulation or moving parts. When combined with a tunable source, it enables frequency-driven beam steering with robust stability [21,22]. Significant efforts have been devoted to this direction across visible, infrared, microwave, and acoustic regimes, utilizing strategies such as geometric phase, optimized meta-atom designs, and diffraction engineering [23–32]. For instance, the design in Ref. [30] operates over 450–850 nm, and geometric-phase PGMs offer intrinsically broadband phase responses [31,32]. Despite these advances, however, the achievable steering range and high-efficiency bandwidth remain limited, and most existing studies have remained largely qualitative. Quantitative analyses that specify the bandwidth improvement for a given dispersion condition are scarce, largely because the bandwidth of PGMs is inherently constrained by the phase tolerance, meta-atom dispersion, and their interplay, factors that make rigorous theoretical analysis challenging. As a result, the relationship between meta-atom dispersion and the attainable bandwidth of the target anomalous order in a passive PGM has yet to be established.

In this work, we address this gap by quantitatively investigating the relationship between dispersion and bandwidth in propagation-phase PGMs, and propose that a dispersionless PGM provides an effective route to high-efficiency frequency–angle beam steering. Our contribution is twofold. Theoretically, rather than pursuing a comprehensive quantitative theory applicable to all dispersion scenarios, we aim to establish a semi-quantitative framework that links the dispersion of constituent meta-atoms to the achievable bandwidth of the target anomalous transmission order in a PGM system. By exploring two limiting cases: an ideal anomalously dispersive PGM and a dispersionless reference PGM, we provide a semi-quantitative benchmark that offers practical guidance for evaluating the bandwidth limits of various dispersive PGM designs. Our analysis reveals that the ideal case yields a theoretical bandwidth of approximately 200% under the efficiency criterion $\eta \geq 0.9$. In stark contrast, the dispersionless PGM, positioned precisely at the transition point between anomalous and normal dispersion, exhibits a finite theoretical bandwidth of about 54.4%. Experimentally, as a proof of concept, we design and fabricate a nearly dispersionless acoustic PGM that achieves high-efficiency frequency–angle beam steering. Designed at 3430 Hz, the device maintains the target anomalous transmission order over 2800–4400 Hz, enabling continuous beam steering from 46.5° to 15.8°, corresponding to an overall steering bandwidth of 344% ($\eta \geq 0.85$) and a field of view of 30.7°. Within this steering range, the target-order transmission efficiency exceeds 90% continuously over 2970–3870 Hz, yielding a high-efficiency bandwidth of 26.3%. Taken together,

Received 23 April 2026; accepted 22 September 2026; published 9 November 2026
© 2026 Chinese Physical Society and IOP Publishing Ltd. All rights, including for text and data mining, AI training, and similar technologies, are reserved.

Check for updates

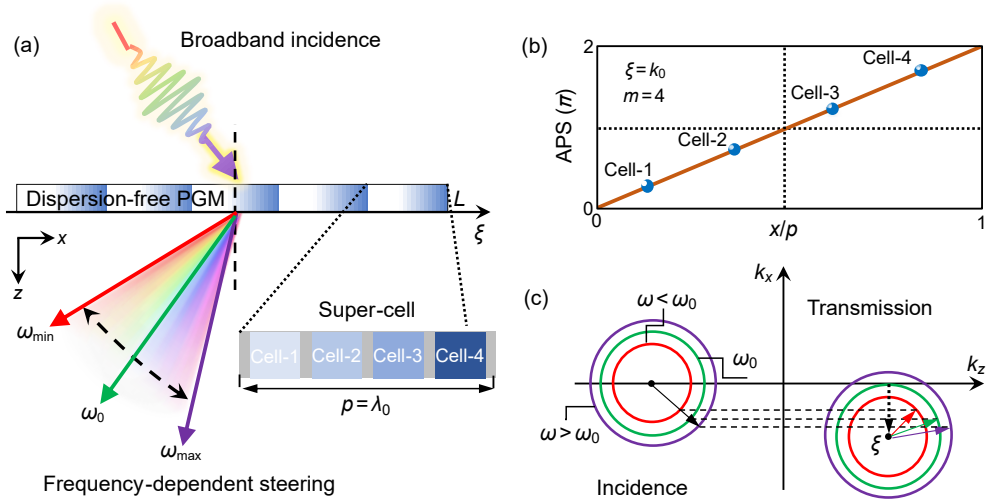

Fig. 1. Principle of dispersionless PGM for frequency–angle beam steering. (a) Schematic of a dispersionless PGM initially designed at a target frequency ω_0, introducing a $\xi = k_0$ along the interface. Under broadband illumination, the PGM diffracts each frequency component into a distinct refraction angle while maintaining high efficiency. (b) In a nearly dispersionless broadband PGM, the APS covering a full 2π range—introduced by the $m = 4$ constituent unit cells within a supercell—remains invariant with frequency, yielding a frequency-independent $\xi = k_0$. (c) Iso-frequency diagram illustrating the principle of frequency-dependent beam steering in a nearly dispersionless broadband PGM.

these results demonstrate a passive, broadly applicable route to high-efficiency frequency-dependent beam steering that requires neither external modulation nor mechanical reconfiguration.

To demonstrate our idea, we begin with the general principle of nearly dispersionless PGM for frequency-dependent beam steering, as illustrated in Fig. 1. The PGM consists of periodically repeated supercells of length p, each comprising $m = 4$ unit cells of width $a = p/m$. Each unit cell (i.e., meta-atom) is made of perfect metal in optics or sound-hard material (gray area) perforated by a subwavelength slit (blue area) of width w. The designed target frequency is ω_0 with corresponding wavelength λ_0. To steer the outgoing wave, the supercell introduces an APS $\Phi(x)$ of complete 2π at transmission interface [Fig. 1(b)], which can be achieved by filling the slits with media of different refractive indices. The refractive index profile in the j-th unit cell is given by $n_j = 1 + (j-1)\,\lambda_0/mL$, which yields an accumulated propagation phase distribution of $\Phi(x) \cong \Phi_j \approx n_j k_0 L$ [37], and the phase difference between two adjacent slits is $\Delta\Phi = \Phi_{j+1} - \Phi_j = 2\pi/m$. When the supercell period satisfies $p = \lambda_0$, this spatially-varying $\Phi(x)$ results in a phase gradient $\xi = \mathrm{d}\Phi(x)/\mathrm{d}x = k_0$ directed along the x axis. For a plane wave incident at an angle $\theta_{\mathrm{in}} < 0°$, the GSL [6] predicts perfect negative refraction, with the refraction angle θ_{t} given by

$$\sin\theta_{\mathrm{t}} = \sin\theta_{\mathrm{in}} + \frac{\lambda_0}{2\pi}\xi. \tag{1}$$

Given $\xi = k_0$, the GSL reduces to $\sin\theta_{\mathrm{t}} = \sin\theta_{\mathrm{in}} + 1$. For $\theta_{\mathrm{in}} = -30°$, this yields $\theta_t = 30°$. The efficiency of this anomalous refraction approaches 100%, a behavior fundamentally distinct from that of conventional grating diffraction [38].

Prior to a detailed examination of the dispersionless scenario, we first consider the ideal broadband PGM. In the ideal case, the phase gradient ξ remains constant and frequency-independent, which requires the phase profile $\Delta\Phi$ to be invariant with frequency. Under this condition, $\xi = k_0$ holds regardless of frequency variations. Consequently, when the incident frequency is shifted to $\omega \neq \omega_0$, perfect negative refraction is still preserved, governed by

$$\sin\theta_{\mathrm{t}}(\omega) = \sin\theta_{\mathrm{in}} + \frac{c}{\omega}\xi, \tag{2}$$

where c is the sound speed. Accordingly, the refraction angle is given by

$$\theta_{\mathrm{t}}(\omega) = \arcsin\left(\sin\theta_{\mathrm{in}} + \frac{\omega_0}{\omega}\right). \tag{3}$$

In the ideal scenario, based on Eq. (3), as the frequency varies continuously over the range $\omega \in (\omega_{\min}, \infty]$ with $\omega_{\min} = \omega_0/(1-\sin\theta_{\mathrm{in}})$, then $\theta_t \in (90°, \theta_{\mathrm{in}}]$, which in principle enables full-angle beam steering. The underlying physics is illustrated by the iso-frequency contours in Fig. 1(c). In this representation, the incident wave is described by a circle of radius $k = \omega/c$ centered at $(k_x, k_y) = (0,0)$. The three incident circles correspond to different frequencies, with the blue circle representing the design frequency ω_0. On the transmission side, the iso-frequency contours are shifted downward by the phase gradient $\xi = k_0$ along the k_x direction, a consequence of momentum conservation imposed by the phase gradient. As shown by the colored arrows in Fig. 1(c), for a fixed incidence angle, the refracted angle varies systematically with frequency.

Having established the frequency–angle relation, we next quantify how the relative dispersion of the constituent meta-atoms constrains the bandwidth over which the target anomalous transmission order can be maintained. Based on coupled-mode theory [27], we calculate the target-order transmission efficiency $\eta = P_{\mathrm{target}}/P_{\mathrm{in}}$, where P_{target} is the power carried by the target anomalous transmission order and P_{in} is the incident power. Two dispersion models are considered under identical conditions. For the ideal anomalously dispersive PGM, the refractive-index profile is prescribed as $n_j(\omega) = 1 + (j-1)\lambda_0\omega_0/(m\omega L)$, which preserves the designed adjacent phase difference $\Delta\Phi = 2\pi/m$ as the frequency varies. For the dispersionless PGM, the effective indices are fixed at their design-frequency values, $n_j(\omega) = n_j(\omega_0)$, and the adjacent phase difference therefore evolves as $\Delta\Phi(\omega) = (\omega/\omega_0)\,(2\pi/m)$. The calculated target-order efficiency spectra of the two models are compared in Fig. 2. The bandwidth is defined as

$$B = \frac{(\omega_{\mathrm{H}} - \omega_{\mathrm{L}})}{(\omega_{\mathrm{H}} + \omega_{\mathrm{L}})/2} \times 100\%, \tag{4}$$

where ω_{L} and ω_{H} denote the bounds of the continuous interval satisfying the specified target-order efficiency criterion. For the ideal anomalously dispersive PGM, $\eta \geq 0.99$ yields a bandwidth of approximately $B = 100\%$. As a practical compromise, an efficiency threshold of $\eta = 0.9$ is already sufficiently high for most applications, and under this condition the corresponding bandwidth is $B = 200\%$, a limit imposed by the intrinsic physics of grating diffraction. By comparison, the dispersionless PGM exhibits a reduced bandwidth of 54.4% under the same criterion of $\eta \geq 0.9$. These results quantitatively show that anomalous relative dispersion broadens the target-order bandwidth, whereas the dispersionless case provides the boundary toward

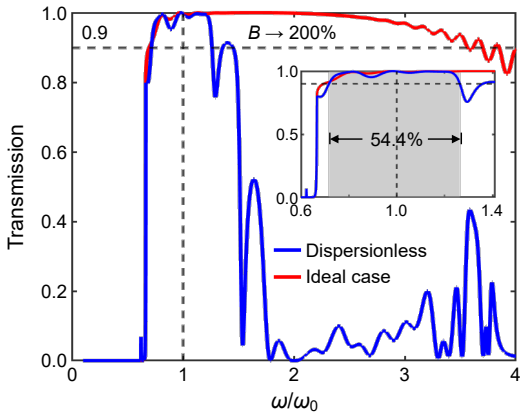

Fig. 2. Quantitative benchmarking of target-diffraction order bandwidth of anomalously dispersive and dispersionless PGMs. Calculated transmission efficiency η of the target anomalous transmission order at $\theta_{in} = -30°$. Both models share the same discrete supercell geometry with $m = 4$ and $p = \lambda_0$. The horizontal dashed line indicates the operating frequency ranges where $\eta \geq 0.9$.

the narrower bandwidth expected for normally dispersive PGMs.

Guided by the theoretical comparison in Fig. 2, we next construct a physically realizable acoustic PGM that approximates the dispersionless reference while maintaining high transmission. As a proof of concept, we employ a subwavelength gradient spoof-fluid-spoof (SFS) acoustic waveguide [39], illustrated in Fig. 3(a). It consists of a pair of parallel rigid plates, each featuring symmetric periodic notches on their top and bottom surfaces. The dispersion relation of the guided acoustic wave in a uniform SFS waveguide (i.e., the rigid plates are of the same height) is

$$\frac{b}{d}k\tan(hk) = \sqrt{\beta^2 - k^2}\tanh\left(\frac{g}{2}\sqrt{\beta^2 - k^2}\right), \tag{5}$$

where β is the propagation constant. Under the subwavelength conditions $hk \ll 1$ and $g\sqrt{\beta^2 - k_0^2} \ll 1$, the approximations $\tan(hk) \approx hk$ and $\tanh(g\sqrt{\beta^2 - k^2}/2) \approx g\sqrt{\beta^2 - k^2}/2$ hold. Substituting these into Eq. (5) yields the simplified dispersion relation,

$$\beta = \frac{\omega}{c}\sqrt{1 + \frac{2b}{gd}h}, \tag{6}$$

which is linear in frequency. The slope of this relation defines the effective refractive index of a uniform SFS waveguide:

$$n_e = \frac{\beta}{k} = \sqrt{1 + \frac{2b}{gd}h}. \tag{7}$$

Within the subwavelength approximation, n_e is independent of frequency and is determined solely by the geometrical parameters. For a fixed set of parameters, n_e can be tuned by adjusting the plate height h. This linear dispersion relation thus provides a foundation for designing dispersionless unit cells.

In the design, the uniform structure is optimized into a gradient configuration to reduce the interfacial wave impedance mismatch and thereby enhance the transmission efficiency of acoustic waves. The design frequency is set to $f_0 = 3430$ Hz, corresponding to a wavelength of $\lambda_0 = 10$ cm. Each unit cell has a period of $p = 10$ cm, with subunit width $a = p/m$, slit width $w = 0.9a$, and total waveguide length $L = 15$ cm. The waveguide comprises 10 notches and 11 rigid plates. The notch width is $b = 1.36$ cm, the spacing between adjacent plates is $d = 1.48$ cm, and the plate thickness is $t = d - b$. The height of the rigid plates follows an exponential distribution from the left edge to the center, given by $y = h - (h - h_0)\frac{1-\exp(5|z|/\lambda_0)}{1-\exp(5L/2\lambda_0)}$, where $h_0 = 0.12$ cm denotes the minimum plate height at the left. This gradient profile enables smooth impedance matching and supports the desired phase engineering across the metasurface.

Based on numerical calculations, figures 3(b) and 3(c) present the transmittance and transmission phase of the designed gradient structure as functions of frequency and height h, respectively. Within the considered frequency range of 2000 Hz to 5000 Hz, the designed SFS structure exhibits extremely high transmittance, exceeding 90% across most of the band. It also demonstrates full 2π phase modulation capability. Specifically, at heights $h = 1.2$, 6.5, 8.5, and 9.6 mm, the phase shifts between adjacent steps differ by $\pi/2$, satisfying the design condition for a PGM with $m = 4$. These four structures serve as meta-atoms that constitute the supercell, as illustrated in Fig. 3(d). Moreover, figure 3(e) shows that these meta-atoms maintain high transmission efficiency even at an incident angle of $-30°$. Figure 3(f) presents the numerically retrieved effective refractive index n_e (solid lines), which remains weakly frequency dependent over the entire operating band. The numerical results are in excellent agreement with the theoretical predictions based on Eq. (7) (dashed lines), confirming an approximately dispersionless response. The slight residual dispersion

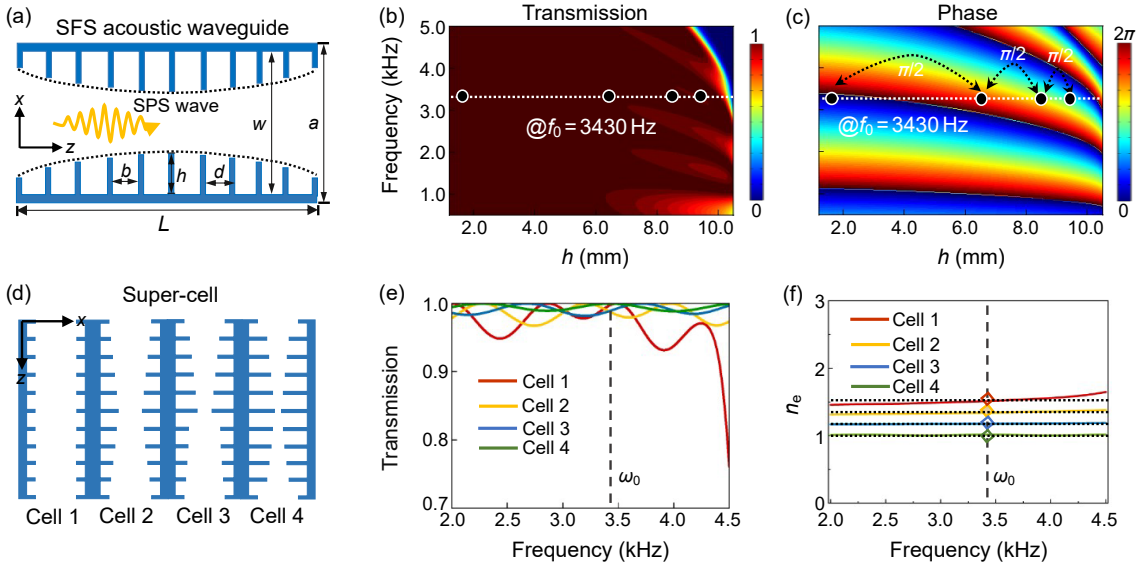

Fig. 3. Acoustic nearly dispersionless PGM design. (a) Schematic of a subwavelength gradient SFS waveguide. (b) and (c) Transmittance and transmission phase of the waveguide shown in (a) as functions of height h and frequency. The asterisks mark four selected heights: $h = 1.2$, 6.5, 8.5, and 9.6 mm. (d) Designed supercell constituting the nearly dispersionless PGM. (e) and (f) Transmittance and effective refractive index n_e of the four unit cells comprising the supercell in (d). The incident angle is $-30°$.

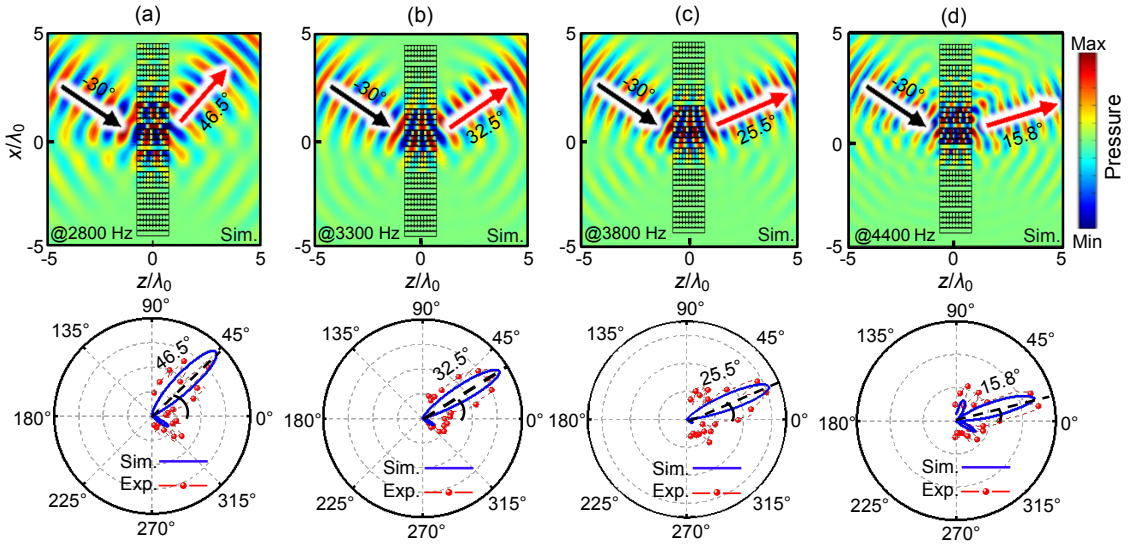

Fig. 4. Frequency-dependent steering performance. Simulated acoustic pressure fields (top panels) and corresponding far-field radiation patterns (bottom panels) demonstrating frequency-dependent beam steering. A Gaussian beam is incident at $\theta_{in} = -30^\circ$ for four representative frequencies: (a) 2800 Hz, (b) 3300 Hz, (c) 3800 Hz, and (d) 4400 Hz. In the bottom panels, the solid curves represent the numerical results, and the circular markers denote the experimental measurements.

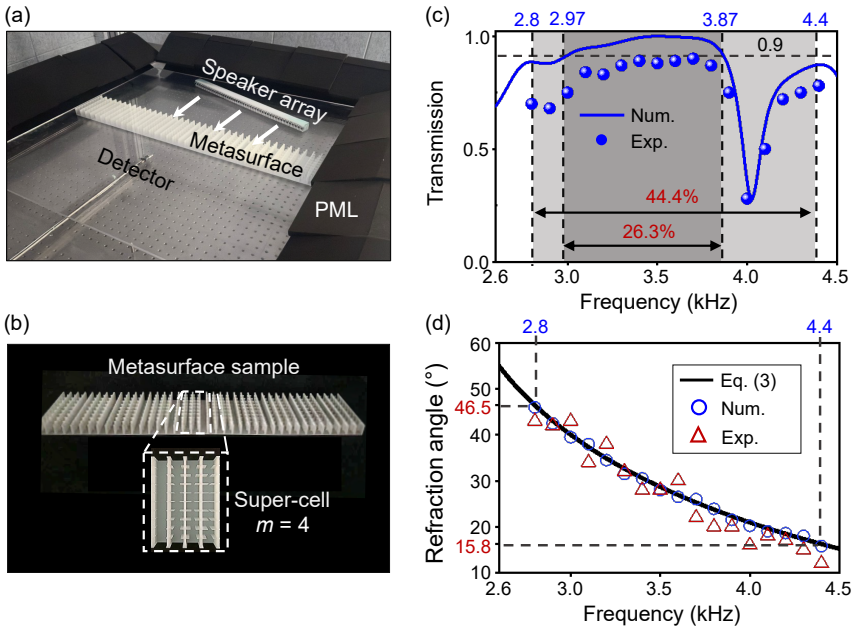

Fig. 5. Experimental setup and validation. (a) Photograph of the experimental setup. (b) Photograph of the fabricated PGM sample; the inset shows a single supercell consisting of $m = 4$ meta-atoms. (c) Transmission efficiency η of the target anomalous transmission order as a function of incident frequency. The solid curve represents full-wave numerical results for the complete finite metasurface, and the circular markers denote experimental measurements. (d) Refraction angle versus incident frequency.

is attributed to near-field coupling between adjacent meta-atoms.

We numerically demonstrate the frequency-dependent steering performance of the designed PGM under an incident Gaussian beam. Figures 4(a)–4(d) show the simulated acoustic pressure fields at 2800, 3300, 3800, and 4400 Hz, respectively. Near-perfect negative refraction is observed at all four frequencies. As the frequency increases, the refraction angle decreases from 46.5° to 15.8°, in agreement with the predicted frequency–angle relation. The corresponding far-field radiation patterns, shown in the bottom panel of Fig. 4, exhibit well-defined refracted beams with high directivity. These results further confirm the frequency-dependent beam-steering functionality of the proposed PGM.

For experimental validation, the designed PGM was fabricated using 3D printing technology. Figure 5(a) shows the experimental setup, and Fig. 5(b) displays the fabricated PGM sample. Sound-absorbing foam was placed around the sample to minimize unwanted reflections and environmental noise. A loudspeaker array served as the acoustic source and was oriented at an incident angle of -30° relative to the sample. A movable miniature microphone was used to map the spatial pressure field by scanning along the x-axis with a step size of 10 mm.

Figure 5(c) presents the target-order transmission-efficiency spectrum of the designed real acoustic PGM, where the solid curve represents numerical simulations, and the circular markers denote experimental measurements. Given the inherent acoustic losses in air during propagation, the two sets of results are in good agreement. The observed dips around 4000 Hz arise from local resonances in the meta-atoms comprising the PGM, which can be mitigated through

further design optimization. In the numerical spectrum, the continuous high-efficiency range, defined by the strict criterion $\eta \geq 0.9$ without interruption, extends from 2970 to 3870 Hz, corresponding to a bandwidth of 26.3%. Meanwhile, the same target anomalous transmission order remains clearly identifiable over the broader range of 2800–4400 Hz, and its steering angle continuously follows the frequency–angle relation predicted by Eq. (3). This range is therefore defined as the overall beam-steering range, corresponding to an overall steering bandwidth of 44.4% ($\eta \geq 0.85$). The local resonance-induced dips only reduce the target-order efficiency but neither alter the selected anomalous transmission order nor disrupt the overall frequency–angle steering behavior. It should be noted that in the actual structure, all constituent unit cells (meta-atoms) exhibit residual dispersion [see Fig. 3(f)], so the designed real PGM is nearly dispersionless or, more precisely, exhibits weak normal dispersion. This is why the overall steering bandwidth under the criterion $\eta \geq 0.9$, is reduced from the ideal value of 54.4% (Fig. 2) to 44.4%, a relatively modest reduction. Figure 5(d) compares the theoretical, numerical, and experimental refraction angles over the overall steering range of 2800–4400 Hz. The theoretical and numerical results indicate that the refraction angle decreases continuously from 46.5° to 15.8°, corresponding to a field of view of 30.7°. The experimental data follow the same frequency-dependent trend and show good agreement with the theoretical and numerical results. Experimental far-field radiation patterns were also measured at 2800, 3300, 3800, and 4400 Hz, as indicated by the circular markers in Fig. 4. Their agreement with the numerical far-field patterns confirms that the same target anomalous transmission order is maintained at these representative frequencies and that its propagation angle follows the predicted frequency–angle relation.

In summary, we have demonstrated theoretically and experimentally that nearly dispersionless PGMs offer a viable route to broadband frequency-dependent acoustic beam steering. Although designed at a target frequency of 3430 Hz, the proposed PGM maintains the target anomalous transmission order over 2800–4400 Hz and continuously steers the refracted beam from 46.5° to 15.8°, corresponding to an overall steering bandwidth of 44.4% ($\eta \geq 0.85$) and a field of view of 30.7°. Within this steering range, the target-order transmission efficiency continuously satisfies $\eta \geq 0.9$ over 2970–3870 Hz, corresponding to a high-efficiency bandwidth of 26.3%. These results demonstrate broadband angular tunability together with high-efficiency acoustic wavefront control. While demonstrated for acoustic waves, the underlying dispersion-engineering approach is broadly applicable to other wave phenomena, including electromagnetic waves. This work establishes a foundation for the study of broadband frequency-dependent wavefront manipulation, such as that involved in orbital angular momentum generation [40], and provides a pathway toward frequency-dependent scanning devices, with promising applications [41] in autonomous driving, navigation, acoustic communication, and medical imaging.

Competing Interests

The authors declare no conflicts of interest.

Data Availability

The data that support the findings of this study are available from the corresponding authors upon reasonable request.

Acknowledgements

This work was supported by the National Key R&D Program of China (Grant Nos. 2022YFA1404301 and 2022YFA1404401), the National Natural Science Foundation of China (Grant No. 12274313), and Collaborative Innovation Center of Suzhou Nano Science and Technology.

References

[1] Sun J, Timurdogan E, Yaacobi A, Hosseini E S, and Watts M R 2013 *Nature* **493** 195
[2] Park J, Jeong B G, Kim S I, Lee D, Kim J, Shin C, Lee C B, Otsuka T, Kyoung J, Kim S, Yang K Y, Park Y Y, Lee J, Hwang I, Jang J, Song S H, Brongersma M L, Ha K, Hwang S W, Choo H, and Choi B L 2021 *Nat. Nanotechnol.* **16** 69
[3] Abdollahramezani S, Hemmatyar O, and Adibi A 2020 *Nanophotonics* **9** 4075
[4] Errico C, Pierre J, Pezet S, Desailly Y, Lenkei Z, Couture O, and Tanter M 2015 *Nature* **527** 499
[5] Ding F, Pors A, and Bozhevolnyi S I 2018 *Rep. Prog. Phys.* **81** 026401
[6] Yu N, Genevet P, Kats M A, Aieta F, Tetienne J P, Capasso F, and Gaburro Z 2011 *Science* **334** 333
[7] Xu Y, Fu Y, and Chen H 2016 *Nat. Rev. Mater.* **1** 16067
[8] Yu N and Capasso F 2014 *Nat. Mater.* **13** 139
[9] Xie Y, Wang W, Chen H, Konneker A, Popa B I, and Cummer S A 2014 *Nat. Commun.* **5** 5553
[10] Tang K, Qiu C, Ke M, Lu J, Ye Y, and Liu Z 2014 *Sci. Rep.* **4** 6517
[11] Berini P 2022 *ACS Photonics* **9** 2204
[12] Wu P C, Pala R A, Kafaie Shirmanesh G, Cheng W H, Sokhoyan R, Grajower M, Alam M Z, Lee D, and Atwater H A 2019 *Nat. Commun.* **10** 3654
[13] Casolaro A, Toscano A, Alù A, and Bilotti F 2020 *IEEE Trans. Antennas Propag.* **68** 1542
[14] Li Q, Kulkarni S P, Sui C, Chen T H, Yan G, Wu R, Chen W, Hung P J, Wu X, Emersic T, Aydin K, and Hsu P C 2026 *Light Sci. Appl.* **15** 38
[15] Zhu S, Cao Y, Fu Y, Li X, Gao L, Chen H, and Xu Y 2020 *Opt. Lett.* **45** 3989
[16] Gu T, Kim H J, Rivero-Baleine C, and Hu J 2023 *Nat. Photonics* **17** 48
[17] Zhuang X, Zhang W, Wang K, Gu Y, An Y, Zhang X, Gu J, Luo D, Han J, and Zhang W 2023 *Light Sci. Appl.* **12** 14
[18] Lin Y, Zou Q, Ning Y, Li J, Xiao P, and Li G 2025 *Adv. Opt. Mater.* **13** e01559
[19] Liu T, Zhang D, Liu W, Yu T, Wu F, Xiao S, Huang L, and Miroshnichenko A E 2024 *Phys. Rev. Appl.* **21** 044004
[20] Jiang G, Wang Y, Zhang Z, Pan W, Chen Y, Wang Y, Chen X, Song E, Huang G, He Q, Sun S, Cui J, Zhou L, and Mei Y 2025 *Nat. Commun.* **16** 1660
[21] Trocha P, Karpov M, Ganin D, Pfeiffer M H P, Kordts A, Wolf S, Krockenberger J, Marin-Palomo P, Weimann C, Randel S, Freude W, Kippenberg T J, and Koos C 2018 *Science* **359** 887
[22] Riemensberger J, Lukashchuk A, Karpov M, Weng W, Lucas E, Liu J, and Kippenberg T J 2020 *Nature* **581** 164
[23] Jung J, Park H, Park J, Chang T, and Shin J 2020 *Nanophotonics* **9** 3165
[24] Yan J, Katsantonis I, Draganidis I, Kourtzanidis K, Monti A, Vellucci S, Barbuto M, Bilotti F, and Kafesaki M 2025 *Phys. Rev. Res.* **7** 013287
[25] Deng M, Cotrufo M, Wang J, Dong J, Ruan Z, Alù A, and Chen L 2024 *Nat. Commun.* **15** 2237
[26] Cao Y, Fu Y, Gao L, Chen H, and Xu Y 2023 *Phys. Rev. A* **107** 013509
[27] Fu Y, Shen C, Cao Y, Gao L, Chen H, Chan C T, Cummer S A, and Xu Y 2019 *Nat. Commun.* **10** 2326
[28] Tanriover I, Dereshgi S A, and Aydin K 2023 *Nat. Commun.* **14** 6484
[29] Li Z, Palacios E, Butun S, and Aydin K 2015 *Nano Lett.* **15** 1615
[30] Devlin R C, Khorasaninejad M, Chen W T, Oh J, and Capasso F 2016 *Proc. Natl. Acad. Sci. USA* **113** 10473
[31] Lin T Y, Huang S H, Chen P C, Lin Y C, Lin C P, Chen S Y, and Wu P C 2025 *Nano Lett.* **25** 10579
[32] Chen W T, Zhu A Y, and Capasso F 2020 *Nat. Rev. Mater.* **5** 604
[33] Wang S, Wu P C, Su V C, Lai Y C, Chen M K, Kuo H Y, Chen B H, Chen Y H, Huang T T, Wang J H, Lin R M, Kuan C H, Li T, Wang Z, Zhu S, and Tsai D P 2018 *Nat. Nanotechnol.* **13** 227
[34] Arbabi E, Arbabi A, Kamali S M, Horie Y, and Faraon A 2017 *Optica* **4** 625
[35] Li B, Lin Q, and Li M 2023 *Nature* **620** 316
[36] Lin Q, Fang S, Yu Y, Xi Z, Shao L, Li B, and Li M 2025 *Nat. Commun.* **16** 4501

[37] Xu Y, Fu Y, and Chen H 2015 *Sci. Rep.* **5** 12219
[38] Larouche S and Smith D R 2012 *Opt. Lett.* **37** 2391
[39] Dong D, Li W, Li X, Liu J, Liu Y, Ji H, Xu Y, and Fu Y 2023 *Appl. Phys. Lett.* **123** 073501
[40] Fu Y, Tian Y, Li X, Yang S, Liu Y, Xu Y, and Lu M 2022 *Phys. Rev. Lett.* **128** 104501
[41] Quan J, Sun B, Wang F, Gao F, Fang X, Gao L, Hang Z, Chen H, Liu Y, Jiang J H, Fu Y, and Xu Y 2025 *Sci. Adv.* **11** eadw1701